Supplementary Information

How a Laser Heats up: Operando Spatio-temporal Heat Dynamics Mapping in Group-IV Lasers

Three-dimensional FIB-SEM tomography and digital twin reconstruction

The internal geometry of the GeSn/SiGeSn microdisk laser was reconstructed using Focused Ion Beam - Scanning Electron Microscopy (FIB-SEM) slice-and-view tomography. Cross-sectional and top-view SEM images obtained during serial sectioning are shown in Video 1. Sequential milling and imaging enabled full three-dimensional reconstruction of the device architecture with an effective spatial resolution of approximately 10 nm.

The reconstruction reveals the detailed morphology of the suspended GeSn/SiGeSn microdisk, Ge pillar, oxide passivation layers and metallic contacts. This experimentally reconstructed geometry was subsequently used to generate a digital twin of the device for the electro-thermal finite-element simulations discussed in the main text.

Supplementary Video 1

Legend: Three-dimensional reconstruction of the GeSn/SiGeSn microdisk laser obtained by FIB-SEM slice-and-view tomography. The video reveals the morphology of the suspended microdisk, Ge support pillar, oxide passivation layers, and metallic contacts.

Electrical calibration of the electro-thermal model

The current-voltage (I-V) characteristics of the GeSn/SiGeSn microdisk laser were measured and compared with electro-thermal simulations at 300 K and 120 K. The simulation at room temperature shows excellent agreement with the experimental data, validating the electrical transport model and the material parameters used in the finite-element simulation. The simulated behaviour at reduced temperature captures the expected shift in the turn-on characteristics, reflecting the temperature dependence of the carrier transport and injection.

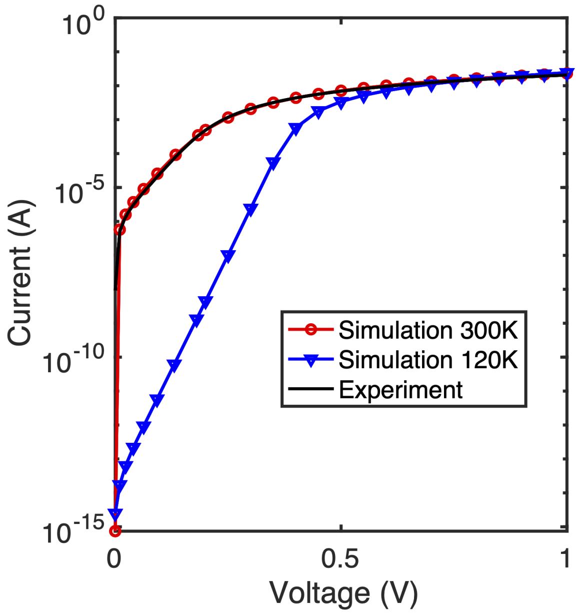

Figure 1: Current–voltage characteristics of the GeSn/SiGeSn microdisk laser diode. Experimental data (black) are compared with electro-thermal simulations (red circles) at room temperature.

Time-resolved diffraction analysis

Time-resolved diffraction curves $I(\theta)$ extracted from the Ge diffraction signal are shown for the contact region (left) and the centre of the pillar (right) at selected delay times. In the pillar region, the diffraction peak shifts gradually with increasing delay, reflecting the slow evolution of the thermal strain associated with diffusive heat transport.

In contrast, the contact region exhibits a pronounced transient broadening and asymmetric deformation of the diffraction curve, particularly within the time window corresponding to maximum heating. The shaded regions indicate angular ranges associated with distinct contributions from the contact and pillar. During electrical excitation, the rapid temperature rise in the contact region produces a temporary separation of diffraction contributions, enabling independent analysis of the two regions.

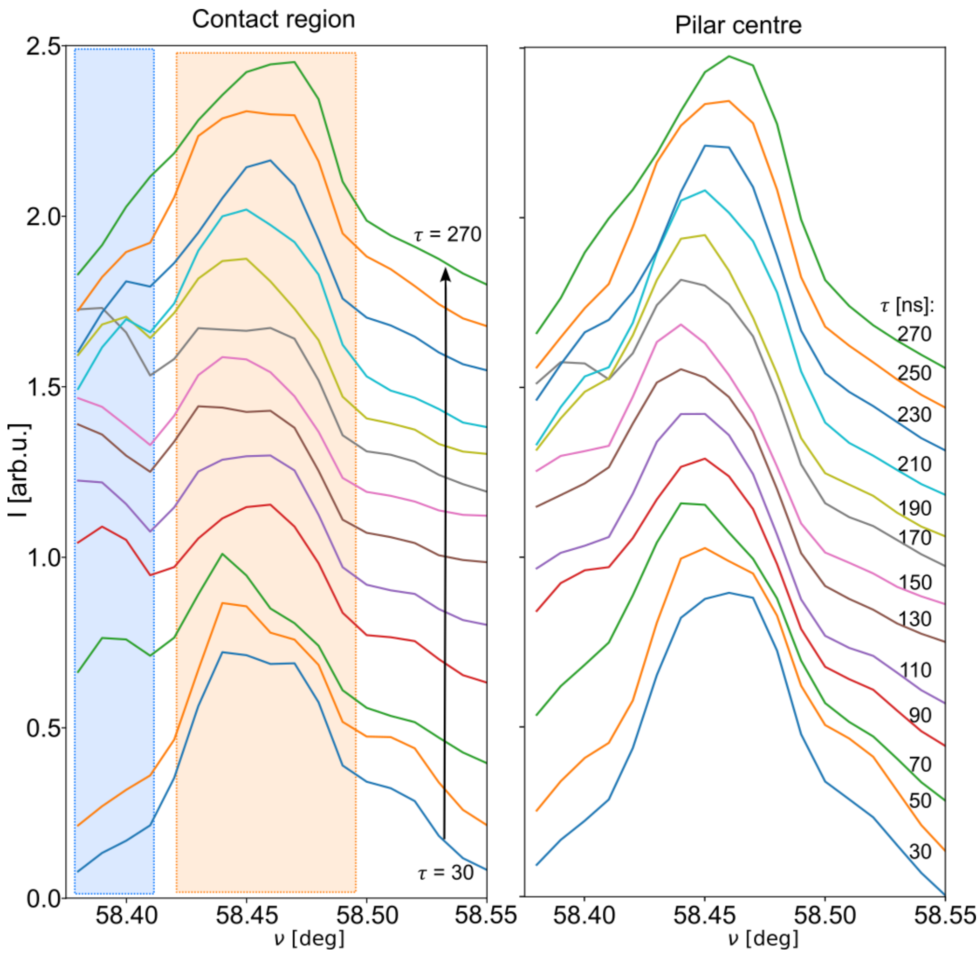

Figure 2: Diffraction curves $I(\theta)$ extracted from the Ge 004 Bragg reflection in the contact region (left) and the pillar centre (right) at selected delay times.

Centre-of-mass strain analysis

To quantify the spatio-temporal evolution of lattice strain across the device, a centre-of-mass analysis of the Ge Bragg diffraction peak was performed. For each spatial pixel and time delay, the angular position of the diffraction peak was determined from the intensity-weighted average of the diffraction curve, providing a robust measure of the local lattice parameter. This approach is particularly suitable in the presence of peak broadening or partial overlap between diffraction contributions from different regions because it captures the average strain within the probed volume without requiring explicit peak separation.

The resulting maps reveal the transient evolution of the thermally induced strain field during electrical excitation and relaxation.

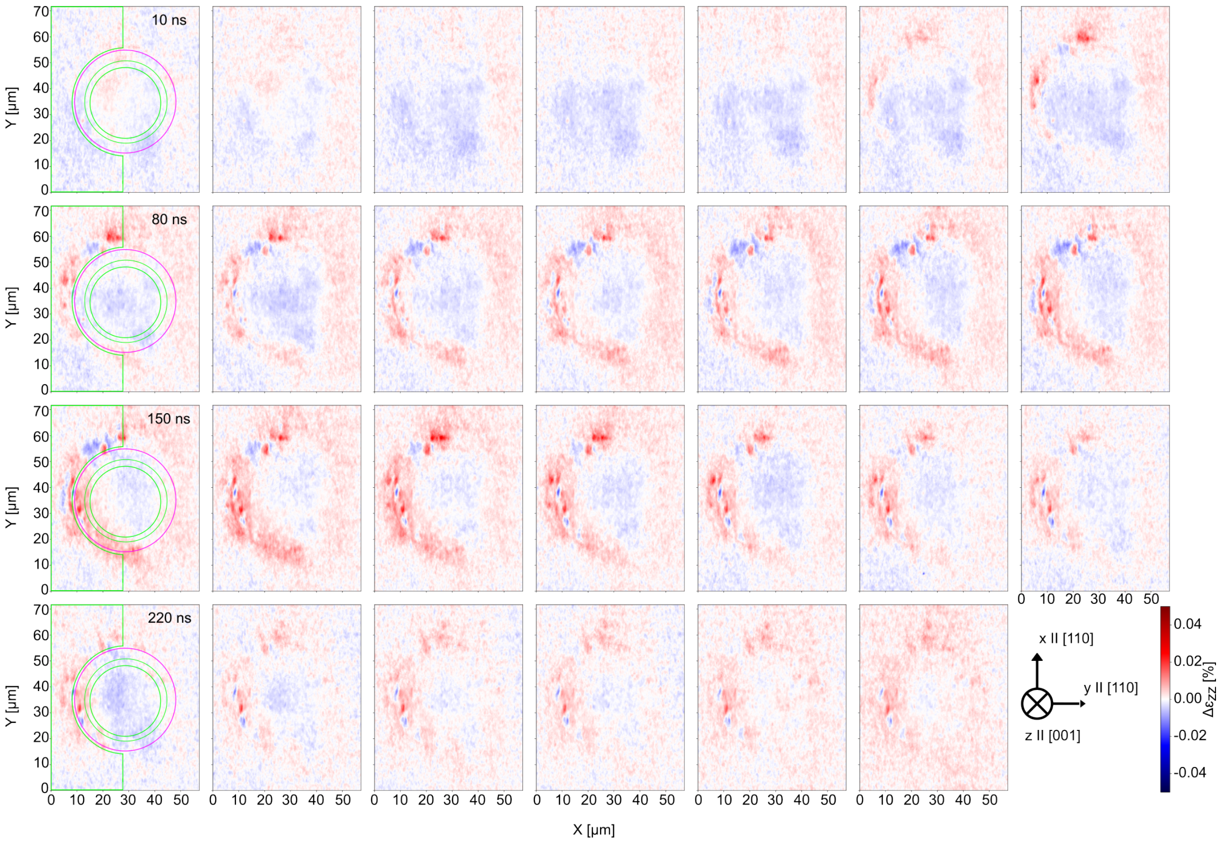

Figure 3: Time evolution of the centre-of-mass position of the Ge 004 Bragg reflection, showing the transient lattice response during electrical pumping.

Contact-resolved strain evolution

To isolate the origin of the transient strain, the analysis was extended to the lower-angle side peak of the Ge diffraction signal, attributed to the p-type contact region. By selectively tracking this diffraction contribution, the strain evolution associated specifically with the contact layer can be resolved independently from the Ge pillar.

The resulting strain maps reveal a strongly localised and rapidly evolving tensile strain response during electrical excitation, consistent with Joule heating induced by current crowding in the contact region.

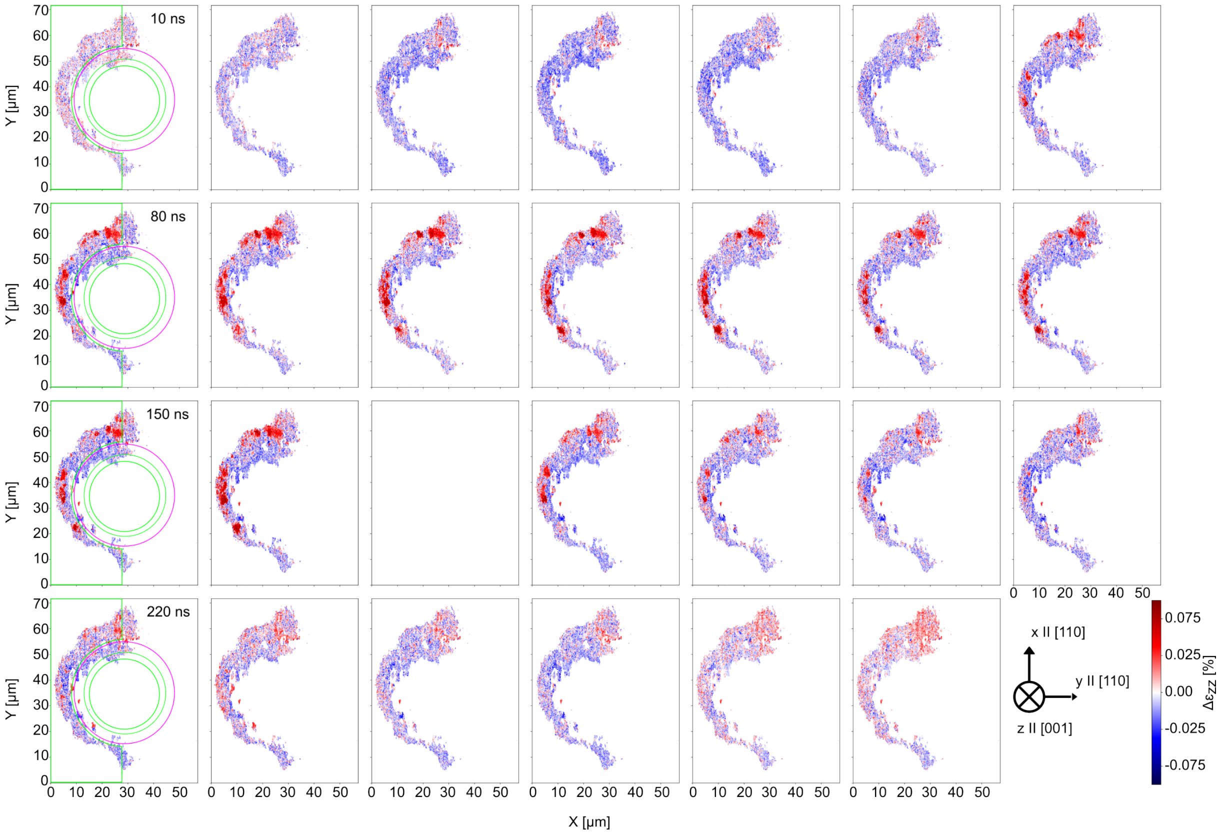

Figure 4: Time evolution of the differential strain extracted from the side peak of the Ge diffraction signal, corresponding predominantly to the p-type contact region.

Pillar-resolved strain evolution

To complement the contact-resolved analysis, the strain evolution associated with the main Ge diffraction peak, attributed to the pillar region, was analysed separately. This contribution reflects the averaged lattice response of the supporting structure and allows the propagation of heat away from the contact to be tracked.

The resulting $\Delta\varepsilon_{zz}(x, y, \tau)$ maps exhibit a weaker and more spatially extended strain distribution compared to the side-peak analysis. The strain develops more gradually following electrical excitation and reaches lower peak amplitudes, consistent with delayed heating driven by thermal diffusion from the contact region rather than direct Joule heating. The spatial pattern is smoother and less localised, reflecting the role of the Ge pillar as the primary heat-spreading pathway.

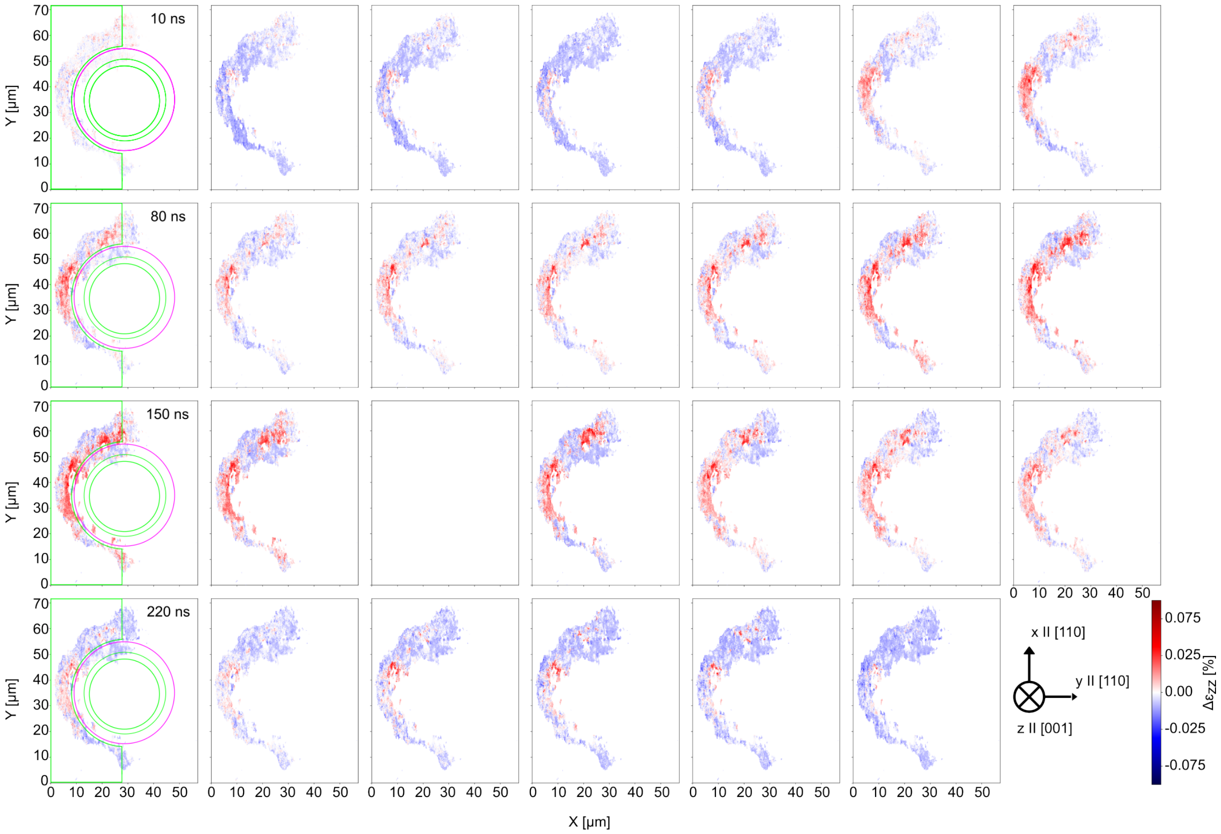

Figure 5: Time evolution of the differential strain extracted from the main Ge diffraction peak, corresponding predominantly to the Ge pillar region.

Simulated current-density distribution

Figure 6 shows the simulated current-density distribution during electrical pumping for a cross-section of the device at $\tau = 140$ ns. Above the active region, the current is predominantly an electron current, whereas below the active region, the transport is dominated by holes.

The simulation reveals strong current crowding in the vicinity of the p-type contact region, producing highly localised Joule heating that directly correlates with the experimentally observed transient strain localisation.

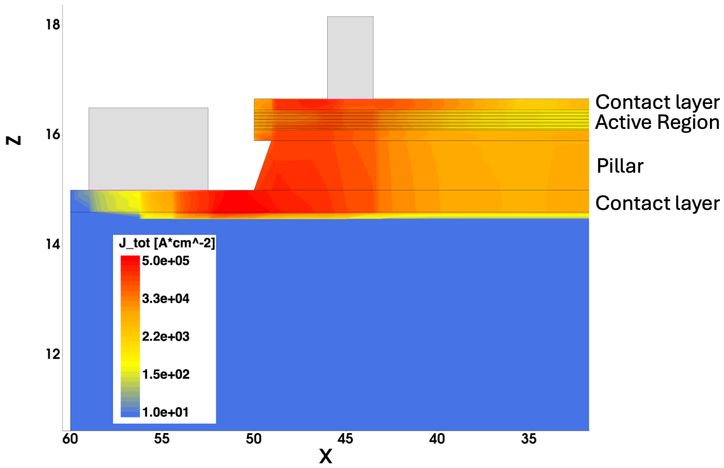

Figure 6: Simulated current-density distribution in a cross-section of the device at $\tau = 140$ ns during electrical pumping.